JACS Au — An Open Access Journal of the American Chemical Society

pubs.acs.org/jacsau
Article

Exploration of Solution-Processed Bi/Sb Solar Cells by Automated Robotic Experiments Equipped with Microwave Conductivity

Chisato Nishikawa, Ryosuke Nishikubo, Fumitaka Ishiwari, and Akinori Saeki*

Cite This: *JACS Au* 2023, 3, 3194−3203
Read Online

ACCESS | Metrics & More | Article Recommendations | Supporting Information

ABSTRACT: Solution-processed inorganic solar cells with less toxic and earth-abundant elements are emerging as viable alternatives to high-performance lead-halide perovskite solar cells. However, the wide range of elements and process parameters impede the rapid exploration of vast chemical spaces. Here, we developed an automated robot-embedded measurement system that performs photoabsorption spectroscopy, optical microscopy, and white-light flash time-resolved microwave conductivity (TRMC). We tested 576 films of quaternary element-blended wide-bandgap Cs−Bi−Sb−I semiconductors with various compositions, organic salt additives (MACl, FACl, MAI, and FAI, where MA and FA represent methylammonium and formamidinium, respectively), and thermal annealing temperatures. Among them, we found that the maximum power conversion efficiency (PCE) was 2.36%, which is significantly higher than the PCE of 0.68% for a reference film without an additive. Machine learning (ML) and statistical analyses revealed significant features and their relationships with TRMC transients, thereby demonstrating the advantages of combining ML and automated experiments for the high-throughput exploration of photovoltaic materials.

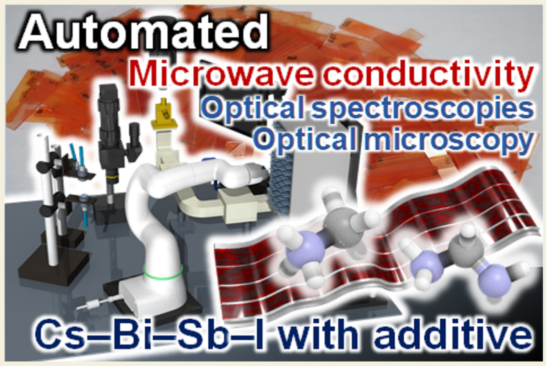

KEYWORDS: *automated experiments with a robot, time-resolved microwave conductivity, solution-processed photovoltaics, cesium−bismuth−antimony−iodide, machine learning, photoabsorption spectroscopy, optical microscopy*

INTRODUCTION

A wave of digital transformation not only propels social service and commercial production but also reenergizes a method of material science research that has traditionally relied on personal experience/idea, serendipitous findings, and trial-and-error experiments.[1,2] Machine learning (ML), which makes use of ever-expanding artificial intelligence (AI) technology, provides an alternative path to a target material and broadens the region of chemical spaces explored.[3−5] To develop an ML model that necessitates a large volume of data, theoretical calculations and manual translations from published works are commonly used.[6−9] However, these data augmentations involve critical issues, such as experimental compatibility, data bias, and inconsistency among the collected data. Automation of experiments that enables high-throughput and high-accuracy measurements is a viable solution to these problems.[10−17] Owing to the recent advancement in robotics and AI, a high-performing and relatively affordable robot is available for automated experiments.[18] Notable examples include the following. (1) A self-wheeling robot that performs sample preparation, evaluation, and experiment design.[19] (2) Optimization of wet processing conditions to maximize conductivity of hole transport material[20] or active layer composition[21] of perovskite solar cells (PSCs). (3) Exploration of blending p-type and n-type semiconductors in organic photovoltaics (OPV).[22,23] (4) Bayesian ML-aided synthesis of organic light emitting diode (OLED)[24] and laser molecules.[25] (5) Closed-loop, self-driven synthesis of metal oxides for an electrode application.[26]

Noncontact mode measurements, such as ultraviolet−visible−near-infrared photoabsorption (PA),[20−25] photoluminescence (PL),[21−25] and Raman spectroscopies,[2,22] are ideal for automated experiments. In this regard, flash-photolysis time-resolved microwave conductivity (TRMC) measurements using a Gigahertz (GHz) electromagnetic wave as a non-contact probe enable a transient photoconductivity ($\Delta\sigma$) measurement that reflects local mobilities and lifetimes of photogenerated charge carriers.[26−28] TRMC has a long history[29,30] and has been used to study the electronic and dielectric properties of inorganic and organic semiconductors.[31−33] Furthermore, transient signals are frequently well correlated with functional outputs, such as power conversion efficiency (PCE) of organic photovoltaic (OPV) devices,[34,35]

Received: September 1, 2023
Revised: October 4, 2023
Accepted: October 5, 2023
Published: October 24, 2023

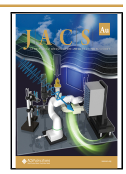

https://doi.org/10.1021/jacsau.3c00519
JACS Au 2023, 3, 3194−3203

PSC,[36−38] and other photovoltaic (PV) devices,[39] as well as photocatalysts.[40] Despite its potential feasibility and fast measurement, TRMC automation has not yet been realized, partly because of the difficulty in precisely integrating optics and electronics.

This study investigated a solution-processed lead-free solar cell composed of the quaternary elements Cs, Bi, Sb and I over a wide range of composition and process parameters using an automated TRMC system coupled with PA and PL spectroscopies and optical microscopy. The need for next-generation solar cells with low-cost, lightweight, and flexible properties is imperative for a carbon-neutral, sustainable society, particularly because lead halide PSCs[41,42] have a high PCE, greater than 25%,[43−46] comparable to that of conventional Si solar cells. Nevertheless, the development of future photovoltaic (PV) materials with diminished toxicity and enhanced stability against moisture and oxygen is essential. Tin halide PSCs are an advanced class of semiconductors with PCEs of ∼15%; however, their instability is a critical issue owing to the easy oxidation of Sn^{2+} to Sn^{4+}.[47−49] In contrast, Bi- and Sb-based halide PV materials[50,51] such as Ag−Bi−I, Ag−Sb−I, Cu−Bi−I, and $Cs_2AgBiBr_6$ display relatively higher stabilities when exposed to air.[39,52−57] However, the vast parameter space in element composition, crystal structures, and processing conditions has left them largely unexplored. We have previously examined ternary, quaternary, and quinary element-mixed PVs ([Na, K, Cs, Rb], [Bi, Sb, In, Ga], [Cu, Ag, Au]) and have found Cs−Bi−Sb−I (Bi:Sb = 1:1) to be a promising candidate for further exploration.[58] Accordingly, in this study, the unexplored conditions concerning the composition (Cs:Bi:Sb), organic salt additives (MACl, FACl, MAI, and FAI, where MA and FA denote methylammonium and formamidinium, respectively), and thermal annealing temperatures were examined in a grid search manner by using an automated system.

RESULTS AND DISCUSSION

Figure 1a shows a schematic of the system composed of a handling robot, PA and PL spectrometers, TRMC optics and electronics, an optical microscope, and a sample cartridge. PA and PL spectroscopies were used to evaluate the bandgap energy (E_g) (Figure 1b). The TRMC comprised an Xe-flash lamp, a signal generator, a resonant cavity at ∼9 GHz, a microwave circuit, a pulse generator, and an oscilloscope. The white light pulse from the Xe-flash lamp is well matched to the sunlight spectrum,[59] making it suitable for evaluating solar cell materials (the operation at 10 Hz, measured intensity ∼0.35 mJ cm^{-2} $pulse^{-1}$ and measured full-width at half-maximum (fwhm) ∼ 2.5 μs that limits the time resolution of the present TRMC system in Figure S1). All instruments were controlled using in-house software, and a typical one cycle measurement is 5 min. As illustrated in Figure 1c, the TRMC transients, obtained by repeating 50 times for the identical sample (Bi_2S_3 powder),[60] demonstrate high reproducibility (standard deviation (STD) of 1.99% for the photoconductivity maximum, $\Delta\sigma_{max}$). An optical microscopic image (256 × 205 μm^2) was automatically analyzed through particle analysis and fast Fourier transform (FFT)-inverse FFT (iFFT) histograms of brightness and dark spots. Figure S2 shows the procedure for these analyses.

Cs−Bi−Sb−I films were formed on a mesoporous TiO_2/quartz substrate by spin-coating a dimethyl sulfoxide (DMSO) solution of CsI, BiI_3 and SbI_3 precursors followed by an

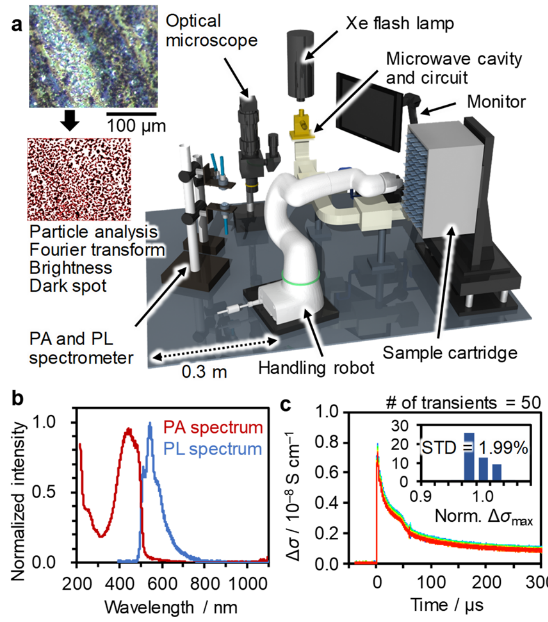

Figure 1. Automated TRMC with PA and PL spectroscopies and optical microscopy. (a) A schematic of the system. An example of optical image along with the particle analysis is appended. (b) PA and PL spectra of conjugated polymer: F8T2 for demonstration. (c) TRMC decays of Bi_2S_3 powder sample for demonstration. The measurements for the identical sample were repeated 50 times, and the decays are superimposed (blue to red). The inset is a histogram of the normalized $\Delta\sigma_{max}$, the STD of which is as low as 1.99%.

antisolvent (toluene) treatment. The total concentration of these precursors was fixed at 1.0 mol L^{-1}, while their compositions were varied as follows: CsI: (BiI_3+SbI_3) ratios of 3:2, 1:1, 2:3, and 1:3 and BiI_3:SbI_3 ratios of 3:2, 1:1, and 2:3, resulting in 12 compositions. Moreover, four types of organic salt additives (MACl, FACl, MAI, and FAI) were incorporated into the solution at concentrations of 50, 100, and 150 mol % relative to the total precursor concentration (e.g., 100 mol % equates to 1.0 mol L^{-1}). These Cs−Bi−Sb compositions were selected based on the Ag−Bi−Sb−I solar cells, where large changes in PCE values and TRMC transients were observed in this compositional range.[39] The above-mentioned additives are often used in lead halide PSCs and their A-site cations (the concentrations were widely changed to examine their effects). Following spin-coating, the films were thermally annealed at a temperature of 100, 150, 200, or 250 °C for 10 min covering a typical temperature (100 °C) to an upper limit of our hot plate, yielding a total of 576 films (= 12 × 4 × 3 × 4; a still image of the films is provided in Figure S3). The TRMC transients, PA spectra, and optical images are shown in Figures S4−S15, S16−S27, and S28−S39, respectively. The current system did not detect the PL of the Cs−Bi−Sb−I films due to their low PL quantum yields less than an instrumental limit (Figure S40).

Figure 2a depicts the two contrasting optical images of the smooth and coarse films, whereas Figure 2b and c depicts their brightness and FFT-iFFT histograms, respectively. The former has a narrower distribution (lower standard deviation) of the smooth film than the coarse film, which could be a useful variable related to film smoothness and beneficial to photovoltaic performance (the smaller, the better). The FFT-iFFT histogram on the other hand shows the opposite trend, with a smooth film having a larger standard deviation than that of the

https://doi.org/10.1021/jacsau.3c00519
JACS Au 2023, 3, 3194−3203

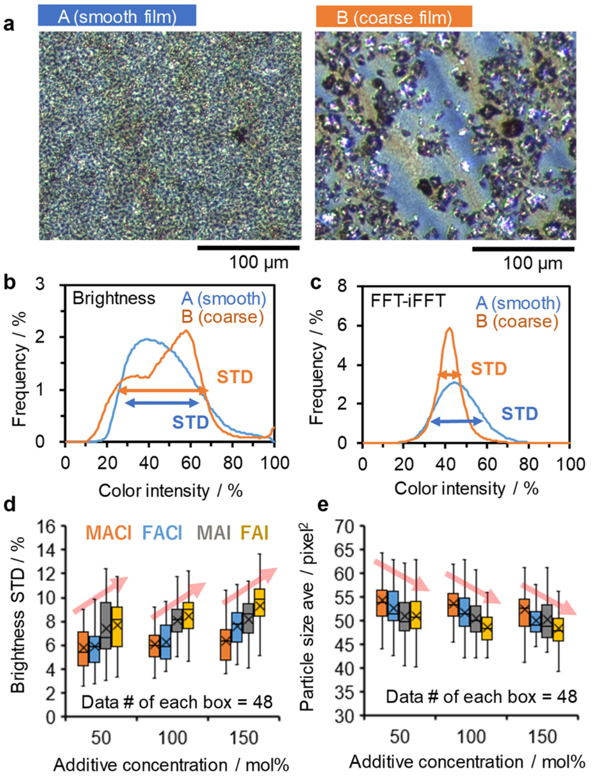

Figure 2. Analysis of optical images. (a) Acquired images of A, a smooth film, and B, a coarse film. (b) A histogram of brightness of gray scale images obtained for A (blue) and B (orange) films. The degree of distribution was quantified by STD (the lengths of arrows does not precisely match the STD values). (c) A histogram of FFT-iFFT-analyzed images acquired for A (blue) and B (orange) films. (d) Box plots of brightness STD categorized by additive and its concentration. (e) Box plots of particle size average (PS_{ave}) categorized by additive and its concentration. The red arrows in (d) and (e) indicate a trend.

coarse film. The brightness STD and average particle size (PS_{ave}) statistics are displayed as box plots in Figure 2d and e, with the types of additives and their concentrations categorized. The brightness STD increased from MACl, FACl and MAI to FAI at each concentration, whereas PS_{ave} decreased in this order. Interestingly, this order corresponds to the molecular weights of the additives (67.5, 80.5, 159.0, and 172.0 g mol^{-1}, respectively), suggesting that a low molecular weight additive leads to a homogeneous, smooth film accompanied by large-sized particles (the PS_{ave} value of 50 $pixel^2$ corresponds to 2 μm^2). Different from the clear impact of the additive chemicals, their concentrations (50−150 mol %) are unlikely to have a large effect on the film morphology.

In contrast to the brightness STD (Figure 2d), the box plot of the TRMC signal ($\Delta\sigma_{max}$) at each additive concentration revealed no distinct trend (Figure 3a). However, for each additive, a moderate increasing behavior of $\Delta\sigma_{max}$ with concentration was observed. When the box plot was categorized by annealing temperature, the results became more scattered (Figure 3b). The highest $\Delta\sigma_{max}$ value was observed at 100 °C for FACl, 200 °C for FAI, and 250 °C for MACl and MAI (the asterisks in the figure). Interestingly, these temperatures are close to the melting points of these additives (85, 242, 230, and 246 °C, according to their catalogue). The translational motion of additive molecules at a high temperature may aid crystal formation and increase the

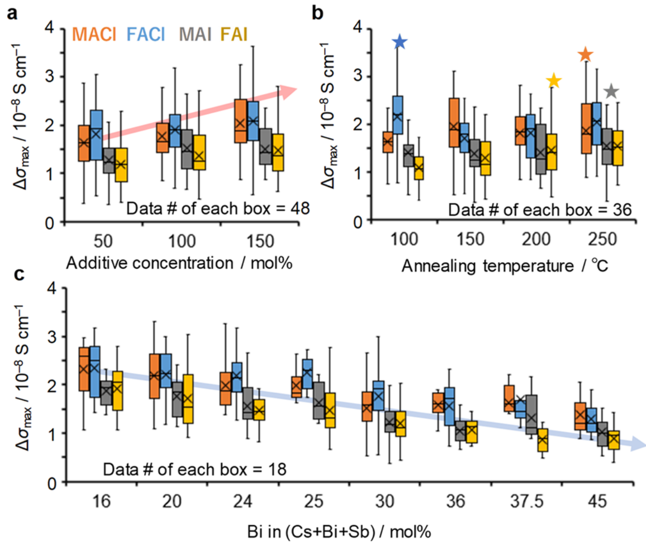

Figure 3. Box plots of $\Delta\sigma_{max}$ categorized by additive. (a) Plots with additive concentration. (b) Plots with thermal annealing temperatures. The highest $\Delta\sigma_{max}$ for each additive is labeled by star symbols. (c) Plots with Bi concentration. The arrows indicate a trend.

$\Delta\sigma_{max}$ values. In contrast, the brightness STD is likely to increase with increasing molecular weight of the additive (Figure S41), similar to Figure 2d. When $\Delta\sigma_{max}$ was categorized by the Bi concentration, it exhibited an overall decreasing trend (Figure 3c). As a complementary response to this trend, $\Delta\sigma_{max}$ seemed to increase with an increasing Cs concentration (Figure S42). We expected E_g to correlate with the Bi or Cs concentrations rather than $\Delta\sigma_{max}$, but this was not the case (Figure S43). This is possibly because the variation of E_g is small (1.71−2.36 eV; average = 2.02 eV; STD = 0.11 eV) in the present process window, and the remaining organic cation of additives may affect E_g in an unexpected manner. In the case of no additive, Cs−Bi−Sb−I (Bi:Sb = 1:1) films exhibited a monotonic increase of E_g from 1.77 to 2.24 eV and shallowing of valence band maximum (VBM) from −5.85 to −5.42 eV with the increase of Cs content (Cs:(Bi+Sb) = 1:3, 2:3, 1:1, 3:2 and 3:1 in Figure S44). This is consistent with the transition from $CsBi_3I_{10}$ (E_g = 1.77 eV) to $Cs_3Bi_2I_9$ (E_g = 2.03 eV) phases with the Cs content.[61] When 100 mol % MACl was added, the $Cs_3Bi_2I_9$ phase (202) peak[61] of X-ray diffraction (XRD) of Cs−Bi−Sb−I (Cs:Bi:Sb = 1:0.5:0.5) underwent a low angle shift from 25.37 to 25.15° (Figure S45). After annealing at 110 and 250 °C, the peak was gradually shifted to a high angle from 25.20 to 25.34°, respectively. Accordingly, the large MA was assumed to be located at the small Cs sites, which affected the E_g values. To quantify the remaining MA cations in the film, Cs−Bi−Sb−I (Cs: Bi: Sb = 1:0.5:0.5) films spin-coated with 100 mol % MACl were dissolved in DMSO-d_6, and the concentration of the remaining MACl was determined using mesitylene as a reference (Figures S46 and S47). Despite the large experimental deviation due to the small amount of the dissolved film (1−2 mg), the concentration of MACl (initially 100 mol %) was decreased from 60 ± 15 mol % at 110 °C annealing to <10 mol % at 300 °C annealing. Thus, a large portion of MA evaporates at high temperatures. Thermogravimetric analysis (TGA) of Cs−Bi−Sb−I films exhibited that the average temperature of 2% weight loss was 262 °C even in the presence of MACl (Figure S48), suggesting

https://doi.org/10.1021/jacsau.3c00519
JACS Au 2023, 3, 3194−3203

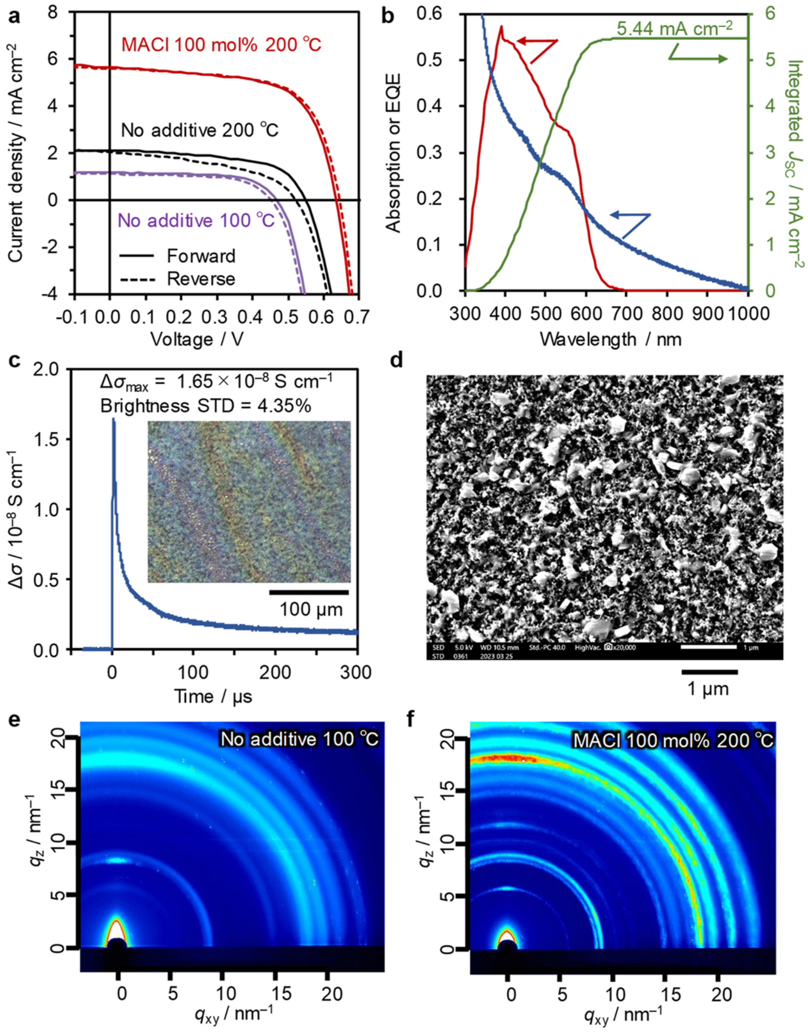

Figure 4. Solar cell characterization of Cs:Bi:Sb = 1:0.5:0.5. (a) *JV* curves with 100 mol % MACl and thermal annealing at 200 °C (red line) and without additive (annealed at 200 °C: black line and 100 °C: purple line). The solid and dotted lines are forward and reverse scans, respectively. (b) Absorption (blue) and EQE (red) curves (left axis). The green curve is the integrated J_{SC} (5.44 mA cm^{-2}). (c) TRMC transient. The inset is the OM image. (d) SEM image. 2D-GIXRD images of (e) no additive and (f) with 100 mol % MACl.

good thermal stability and mostly unchanged metal compositions.

Upon characterization of the PV devices, we chose 40 kinds of films out of 576 films to cover a wide range of Cs−Bi−Sb−I compositions, four types of additives, their concentrations, and thermal annealing temperatures (Tables S1 and S2). Notably, we obtained the PCE of 2.36% for Cs:Bi:Sb = 1:0.5:0.5 processed with 100 mol % MACl and thermal annealing at 200 °C (Figure 4a and Table 1), which was significantly improved from PCE = 0.68% for the same condition without additive. Along with a good match of J_{SC} between 1 sun (5.65 mA cm^{-2}) and the external quantum efficiency (EQE) spectrum (5.44 mA cm^{-2} in Figure 4b), a small hysteresis (hysteresis factor = (reverse−forward)/reverse = 0.02) was also noticeable. The EQE onset is located at about 660 nm, which is relevant to its E_g (1.92 eV, 646 nm), as determined by automated PA spectroscopy. The VBM (−5.48 eV) evaluated by photoelectron yield spectroscopy (PYS) and CBM (−3.56 eV = VBM + E_g) are well-matched with the polymer hole transport material (PBDB-T) and mpTiO_2, respectively (Figure S49). As shown in Figure 4c, this optimal film has a relatively high TRMC signal ($\Delta\sigma_{max}$ = 1.65 × 10^{-8} S cm^{-1}) and good homogeneity in the optimal microscope image (brightness STD = 4.35%). Nonetheless, scanning electron microscopy (SEM) observations revealed rough multicrystalline features on a scale of hundreds of nanometers (Figure 4d), which are associated with the long tail of the PA spectrum caused by light scattering. The SEM-observed morphology was superior to that of the reference without additives,[58] and the cross-sectional SEM images revealed no distinct pinholes (Figure S50). However, the current results indicate that the submicrometer-scale morphology of this film has a large scope for improvement in terms of homogeneity and smoothness, implying the possibility for further research.

Two-dimensional grazing-incidence X-ray diffraction (2D-GIXRD) measurements showed drastic changes in intensity and orientation. The film without additive and annealed at 100 °C exhibited a nonorientated arch profile (Figure 4e), whereas the optimal film with MACl and annealed at 200 °C showed increased intensities in the out-of-plane direction (OOP, Figure 4f). In particular, the peak at the scattering vector (q) ~ 17.9 nm^{-1} attributed to (202) of the $Cs_3Bi_2I_9$ phase[61] is prominent and concentrated in the OOP direction. The increase in the orientation and diffraction intensity was

https://doi.org/10.1021/jacsau.3c00519
JACS Au 2023, 3, 3194−3203

Table 1. Solar Cell Characterizations (FTO/compactTiO$_2$/mpTiO$_2$/Cs-Bi-Sb-I/PBDB-T/Au)[a]

Cs:Bi:Sb	Additive	Additive conc. (mol %)	Anneal temp. (°C)	E_g (eV)	PCE[b] (%)	J_{SC}[b] (mA cm^{-2})	V_{OC}[b] (V)	FF[b]	HI[c]
1:0.5:0.5	none	none	200	2.00	0.51 ± 0.09 (0.68)	2.04 ± 0.2 (2.12)	0.519 ± 0.033 (0.550)	0.486 ± 0.077 (0.584)	−0.25 ± 0.19 (−0.29)
1:0.5:0.5	MACl	100	200	1.92	2.22 ± 0.09 (2.36)	5.31 ± 0.2 (5.65)	0.647 ± 0.013 (0.634)	0.646 ± 0.01 (0.643)	0.03 ± 0.06 (0.02)
2:1.8:1.2	FACl	50	250	2.04	0.72 ± 0.05 (0.81)	1.82 ± 0.11 (2.10)	0.679 ± 0.013 (0.687)	0.584 ± 0.022 (0.557)	−0.01 ± 0.09 (0.01)
2:1.5:1.5	MAI	50	250	1.87	0.62 ± 0.07 (0.72)	1.75 ± 0.15 (1.96)	0.631 ± 0.014 (0.636)	0.558 ± 0.038 (0.581)	−0.05 ± 0.16 (−0.07)
1:1.2:1.8	FAI	50	250	2.06	0.78 ± 0.11 (0.95)	2.11 ± 0.24 (2.42)	0.658 ± 0.031 (0.691)	0.564 ± 0.018 (0.565)	−0.03 ± 0.18(−0.08)

[a]The optimal results for each additive are listed. The complete list is provided in Table S2. [b]The values in brackets are the maximum values, while the value with deviation is the average of the forward and reverse scans in multiple (8−9) devices. [c]Hysteresis factor (HI) is calculated as (reverse−forward)/reverse.

promoted by first increasing the annealing temperature and then increasing the MACl concentration (Figure S51). These effects became smaller when the Cs concentration (Cs/(Bi+Sb)) was low (<0.5), suggesting a highly crystalline nature of the Cs-rich component at high temperatures (Figure S52).

The second highest PCE of 2.15% was obtained with the neighbor parameters, namely, Cs:Bi:Sb = 1:0.75:0.75 with 150 mol % MACl and annealing at 250 °C. We also performed device characterizations and TRMC measurements for the small-step (by 25 °C) and wide temperature range (110−300 °C) for the optimal Cs−Bi−Sb−I composition (Figure S53 and Table S3). As a result, 200 °C was found to be optimal, and the device performance dominated by J_{SC} and TRMC results were well-correlated. In the case without additive, 200 °C was also optimal, while its PCE was less than 0.68% (Table S4). Although the optical bandgap did not change with increasing annealing temperature, the photoabsorption edge became sharp (Urbach energy decreased from 0.30 to 0.25 eV), and the crystallite size calculated from the XRD peak width increased from 25 to 55 nm (Figure S54). Therefore, a high annealing temperature leads to a higher crystallinity and possibly better charge transport. We also examined other additives (NH_4Cl and NH_4SCN) for Cs−Bi−Sb (1:0.5:0.5); however, their TRMC photoconductivities were much lower than those of MACl (Figure S55). This led to PCEs of less than 1% (0.93% for NH_4Cl and 0.49% for NH_4SCN, as shown in Figure S56 and Tables S5 and S6) and moderate crystallinity (Figure S57).

A random forest (RF) ML model was constructed based on 40 data points, with the PCE as the objective variable and 13 parameters obtained from the automated experiments and process parameters (additive, concentration, temperature, and Cs and Bi concentrations) serving as the explanatory variables. As shown in Figure 5a, the correlation coefficient (r) evaluated using the leave-one-out (LOO) method was moderate at 0.69. This low prediction accuracy in turn means that an alternative approach instead of ML should be examined, which is discussed in the next paragraph. The feature importance depicted by the red bars in Figure 5b revealed that E_g was the most important parameter, followed by the additive category, annealing temperature and $\Delta\sigma_{max}$. The blue bars in the same figure represent the observed data variation in STD (%), whereas nonobserved parameters, such as additive category, annealing temperature, additive, and Bi/Cs concentrations, are not displayed. Consequently, $\Delta\sigma_{max}$ and brightness STD are the parameters that exhibit a high importance value and large data variation (Figure 5c and Figure S58).

We then discuss the correlation and distribution of these parameters in addition to the superposition of the experimental PCE values. The map of E_g vs $\Delta\sigma_{max}$ in Figure 5d is evidently scattered, and the experimental PCE plots are also dispersed across the whole range of the map. By contrast, a counterplot trend can be seen in the brightness STD versus $\Delta\sigma_{max}$ plot (Figure 5e), despite the fact that the data are widely distributed across the map. The bottom right direction, corresponding to low brightness STD and high $\Delta\sigma_{max}$, namely, smooth and highly photoconductive material, is relevant to the high PCE devices. In fact, as shown in Figure 5f and Figure S59, high-performing lead halide perovskite has a lower brightness STD (3.57%) and one-order higher $\Delta\sigma_{max}$ value (3.87 × 10^{-7} S cm^{-1}) than Cs−Bi−Sb−I (Figure 4c and Figure S60), corroborating a logical direction of exploration by the automated, fast screening of PV materials. Furthermore, the

https://doi.org/10.1021/jacsau.3c00519
JACS Au 2023, 3, 3194−3203

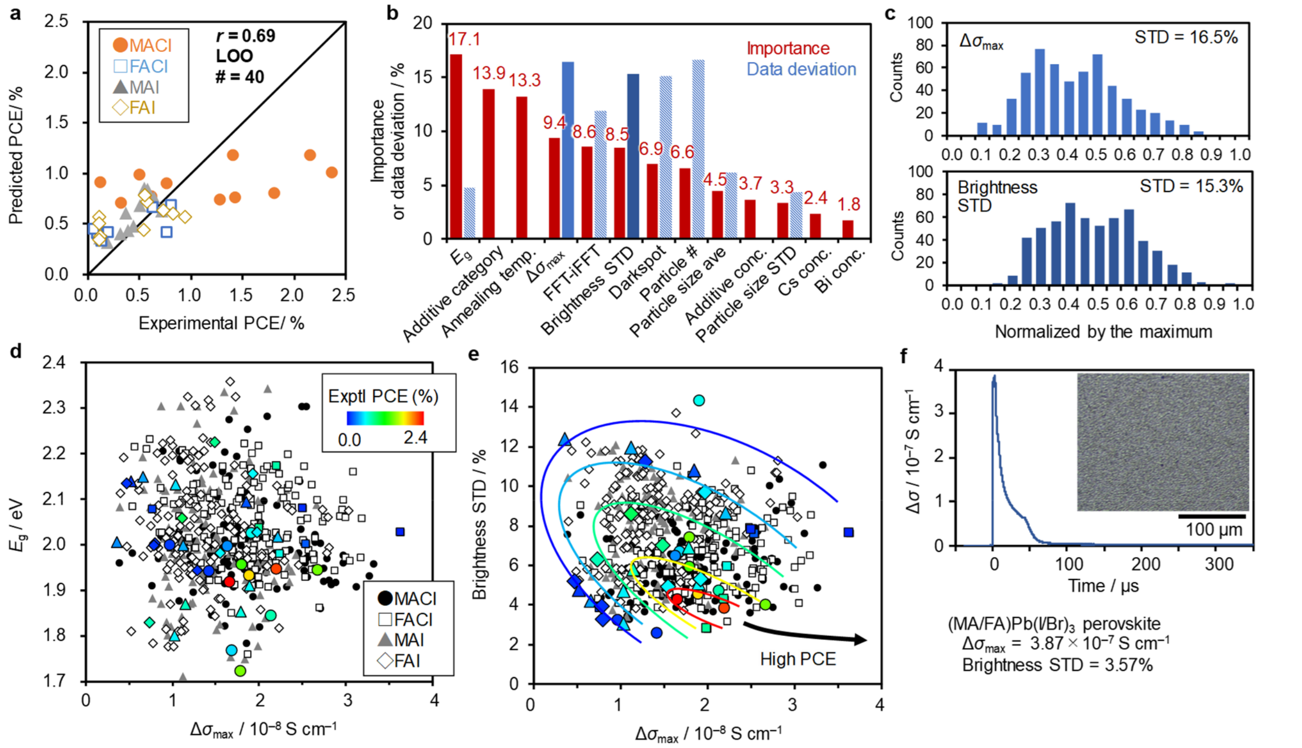

Figure 5. ML and statistical analyses of the PCEs of PV devices. (a) Correlation between predicted and experimental PCE obtained from the RF model (r = 0.69, leave-one-out, number of data: 40). The additives are categorized according to each symbol. (b) Importance (red bars with values) of RF model sorted in descending order. The data deviation (STD) of each parameter is appended (blue bars). The dark and light blue bars corresponds to the histograms in (c). Those without blue bars indicate that their deviations were determined by sample preparation. (c) Histograms of $\Delta\sigma_{max}$ (upper panel) and brightness standard deviation (STD) (lower panel) with STD values. (d) E_g vs $\Delta\sigma_{max}$ plot. (e) Brightness STD vs $\Delta\sigma_{max}$ plot. The colored lines are counterplots drawn using an eye guide. The black arrow indicates the direction of high PCE. In (d) and (e), the additive is categorized by each symbol. The color plots correspond to experimental PCE values. (f) TRMC transient of lead-halide perovskite: $(MA/FA)Pb(I/Br)_3$. The optical images were then superimposed. The $\Delta\sigma_{max}$ and brightness STD values are presented, which matches the extrapolated region in (e).

$\Delta\sigma_{max}$ induced by a white light pulse incorporates the PA property of a film and carrier lifetime, reinforcing its association with PCE.[59] We also examined the FFT-iFFT STD versus $\Delta\sigma_{max}$ plot (Figure S61) but discovered no such a trend. The dark spot, particle number, and PS_{ave} are also other parameters acquired in the optical image analysis. They are approximately correlated with the brightness STD with r = 0.637, − 0.569, and −0.537, respectively (Figure S62); thus, the sole selection of the brightness STD rather than these parameters is reliable and effective. In addition, RF regressions of the brightness STD, $\Delta\sigma_{max}$ and E_g were performed using the 576 data set that includes observed parameters ($\Delta\sigma_{max}$, OM parameters, etc.) and synthetic conditions (Cs concentration, Bi:Sb ratio, etc.), exhibiting the moderate or poor r values of 0.64, 0.70, and 0.18, respectively (Figure S63). This means that experimental screening is more effective than the virtual one to find a high-performing active layer. Based on these findings, we foresee that the integration of our automated measurement system with an automated film processing system and MI (e.g., Bayesian inference) would further accelerate a discovery of PV materials and processing.

CONCLUSION

We developed an automated, noncontact measurement system that can perform PA and PL spectroscopy, optical microscopy, and Xe-flash TRMC within approximately five min for a single sample. Using this system, we investigated solution-processed lead-free photovoltaic materials composed of Cs−Bi−Sb−I with varying Cs:Bi:Sb compositions, organic halide additives, and thermal annealing temperatures. Through the automated experiments of 576 films and device characterization of 40 solar cells, we observed a PCE of 2.36% for Cs:Bi:Sb = 1:0.5:0.5 with 100 mol % MACl and thermal annealing at 200 °C, significantly enhanced compared to the reference (0.68%) without additive. Moreover, the brightness STD and $\Delta\sigma_{max}$, derived from the optical microscopic image analysis and TRMC, respectively, were proposed as a vial indicator for identifying high-performing PV materials. The unique automated robotic experiments and findings presented in this study will benefit scientific research on PV materials by accelerating the discovery process.

EXPERIMENTAL SECTION

Automated Measurement System

A handling robot (DensoWave Corporation. Cobotta) was controlled by using in-house software through the ORiN2 (Open Robot/Resource Interface for Network version 2) interface. A deuterium and halogen light source was obtained from Ocean Insight Corp. A DH-2000-BAL instrument was utilized as the probe for PA spectroscopy, and light was guided through an optical fiber and a collimated lens. A LED laser (Ocean Optics Corp. LSM-365A), which was transmitted through an optical fiber, served as the excitation source for PL spectroscopy (λ_{ex} = 365 nm). The transmitted white light of the PA and the emitted light of the PL were monitored by an Ocean Optics Corp. HR4000CG-UV-NIR spectrometer (200−1100 nm) equipped

https://doi.org/10.1021/jacsau.3c00519
JACS Au 2023, 3, 3194−3203

with a collimating lens and optical fiber. A typical total integration time was 0.1 and 10 s for PA (reference, signal and background) and PL (signal and background), respectively. Optical microscope (Shodensha Corp.) NSH130CSLT, with coaxial exposure optics, was embedded, where the focus point at the maximum Laplacian variation of image was scanned by controlling the *z*-axis of a stepping motor stage (Sigma-Koki Corp. OSMS60−10ZF with 1 μm accuracy). Brightness was automatically adjusted after autofocusing by changing the exposure time of a USB camera. The size of the optical image was 1280 × 1024 pixels, which corresponded to 256 × 205 μm (0.200 μm pixel^{-1}), and was calibrated using a microscaler (Olympus Corp. OB-M, with a minimal 0.01 mm scale). A sample cartridge was designed to place five substrates in each row (number of rows = 11; thus, 55 samples for one batch). A robot picked up and returned a sample at a fixed position, while the sample cartridge was equipped with stepping motor stages (Sigma-Koki Corp. models of OSMS26−100X and OSMS26−200Z) were moved in the horizontal and vertical directions. These stepping motor stages were controlled using a pulse generator and driver of Sigma-Koki Corp. model HSC-103. The TRMC comprised a Xe-flash lamp (Hamamatsu Photonics Corp. L7684, 250−1100 nm) and a microwave signal generator (Rohde Schwarz Corp. SMB-100A, ∼3 mW), a resonant cavity (TE_{102}, ∼ 9 GHz), a microwave circuit (isolator, circulator, waveguide, amplifier, and detector),[33,59] a pulse generator to trigger the Xe-flash lamp and synchronize with the signal (Quantum Composers Corp. Sapphire 9212) and an oscilloscope (a Tektronix Corp. MSO44). A quartz substrate was inserted into the resonant cavity through a pipe attached to the widest area (the electric field of the microwaves was parallel to the in-plane direction of the film). All instruments were controlled using in-house software developed using Microsoft Visual Studio 2022 (Visual C++). After the sample was placed in the resonant cavity, the resonant frequency was automatically scanned and tuned to an accuracy of 1 kHz. The white light pulse (10 Hz, ∼0.35 mJ cm^{-2} pulse^{-1}, fwhm ∼2.5 μs) from a Xe-flash lamp was exposed to the sample and averaged for ∼9 s (>80 pulses). The photoconductivity was calculated through $\Delta\sigma = A^{-1}\Delta P_r P_r^{-1}$, where A is the sensitivity factor, P_r is the reflected microwave power, and ΔP_r is the change in P_r upon exposure to light. The experiments were performed in the air at 25 °C. The typical one-cycle time (sample pick-up, PA and PL spectroscopy, optical microscopy, TRMC, and sample return) was 5 min. Image analysis was performed automatically using the OpenCV module embedded in the measurement software. The brightness STD was calculated from the histogram of a grayscale image normalized by the maximum (255). The average value of the histogram was excluded from the analysis because the brightness of the image was tuned for each film during the measurement. Furthermore, a grayscale image was analyzed using FFT and reconstructed using iFFT through a low-pass filter (<95% of the maximum frequency) and a high-pass filter (>10% of the maximum frequency). The STD value of the FFT−iFFT histogram was calculated in the same manner. Particle size analysis was conducted on a grayscale image after the Gaussian blur (size = 3 × 3 pixels), adaptive threshold (threshold = 99, block size = 12 × 12 pixels) and edge-extraction processes. The average particle size and STD values were calculated in the same manner, and the number of particles was counted. Dark spot analysis was performed on a black-white image (threshold = 60 in 255), and the percentage of black pixels was calculated. A movie of the measurements and analysis is provided in the Supporting Information.

Materials

The precursors CsI (99.0%), BiI_3 (99.998%), and SbI_3 (99.998%) were procured from Sigma-Aldrich and used without further purification. MAI (MA: CH_3NH_3), MACl, FAI (FA: $(NH_2)_2CH$), and FACl of solar cell grade were purchased from Tokyo Chemical Industry Co., Ltd. (TCI, Japan) and used as received. Additional perovskite precursors of PbI_2, $PbBr_2$, and MABr in solar cell grade were purchased from TCI. DMSO, *N*,*N*′-dimethylformamide (DMF) and toluene (Wako-Fuji Film Industries Ltd., WFFI, O_2 < 1 ppm, H_2O < 0.001%) were used as received. The highest grade chlorobenzene (CB) was acquired from WFFI and used as received. PBDB-T, a hole transport materials (HTMs) was obtained from 1-Materials Inc. DMSO-d_6 (99.9% D) was purchased from Kanto Chemical Co., Ltd. F8T2 (poly[[2,2′-bithiophene]-5,5′-diyl(9,9-dioctyl-9H-fluorene-2,7-diyl)]) and Bi_2S_3 powders were purchased from Sigma-Aldrich.

General Measurement

The PYS of the films on F-doped SnO_2 (FTO) glass was assessed using a Bunko Keiki BIP-KV202GD instrument under vacuum (<10^{-2} Pa). XRD was performed using a Rigaku Corp. MiniFlex-600 instrument (Cu K_α radiation: λ = 1.54 Å) in an ambient, room temperature atmosphere. Field-emission scanning electron microscopy (FE-SEM) was performed using a JEOL JSM-IT700HR instrument (5 keV, 50 μA). The photoabsorption spectra of some of the films were measured using a Jasco V-730 UV−vis spectrophotometer. 2D-GIXRD was conducted at the BL46XU or BL13XU beamline of the Japan Synchrotron Radiation Research Institute, using 12.39 keV (λ = 1.00 Å) X-rays. ^{1}H nuclear magnetic resonance (NMR) (400 MHz) spectra were measured by using a JEOL JNM-ECZS400 spectrometer at room temperature. Thermogravimetric analysis (TGA) was performed using a Shimadzu TGA-50. A PL spectrum measurement to confirm no emission from a Cs−Bi−Sb−I film (a low PL quantum yield) was performed using a Jasco FP-8300 spectrometer.

Film Preparation and Solar Cell

After cleaning the FTO/glass with detergent, acetone, isopropyl alcohol, and deionized water, a compact TiO_2 layer (c-TiO_2) was deposited onto the FTO by spray pyrolysis using a solution of titanium diisopropoxide bis(acetylacetonate) (TCI) in ethanol (1:14 v/v) at 450 °C. A 200 nm-thick mesoporous TiO_2 (mp-TiO_2) layer (average particle size: 20 nm, anatase) was deposited onto the compact TiO_2 layer by spin-coating (slope 5 s, 5,000 rpm for 30 s, slope 5 s) a diluted TiO_2 paste (30NR-D, GreatCell Solar Ltd.) in ethanol (paste:ethanol = 1:7 w/w), followed by sintering at 500 °C for 20 min. A quartz substrate with mp-TiO_2 was prepared in the same fashion as the automated experiments. A 1.0 M DMSO solution of CsI, BiI_3, and SbI_3 at the designated stoichiometry was prepared in a N_2-filled glovebox (O_2 < 0.1 ppm, H_2O < 0.1 ppm). The solutions were stirred for more than 1 h at 80 °C. Subsequently, the precursor layer was formed by spin-coating the DMSO solution (slope 1 s, 4,000 rpm for 50 s, slope 3 s). At 40 s, antisolvent treatment (toluene) was applied by slowly dropping 0.2 mL solvent onto a rotating substrate. The resultant film was annealed at 100−300 °C for 10 min, affording a 100 nm-thick photoactive layer. For the solar cells, HTM without dopants (PBDB-T) was deposited by spin-coating a CB solution (10 mg mL^{-1}) at 2000 rpm for 30 s, yielding a typically 70 nm thick HTM. Subsequently, 70 nm-thick Au electrode was thermally deposited in a vacuum chamber. The size of the active area was determined by using a shadow mask (0.04 cm^2). Current−voltage curves were measured by using a source meter unit (ADCMT Corp., 6241A) under AM 1.5 G solar illumination at 100 mW cm^{-2} (1 sun, monitored by a calibrated standard cell, Bunko Keiki SM-250 KD) from a 300 W solar simulator (SAN-EI Corp., XES-301S). The voltage scan (forward and reverse) was performed at a scan speed of 0.08 V s^{-1}. *JV* curves of a device without encapsulation were measured in air at 25 °C. External quantum efficiency (EQE) spectra were measured using a Bunko Keiki model BS-520BK equipped with a Keithley model 2401 source meter (a scan speed of 10 nm s^{-1}). The monochromatic light power was calibrated using a silicon photovoltaic cell (Bunko Keiki model S1337−1010BQ). A reference lead halide perovskite film on quartz was prepared by spin-coating a 1.4 mol L^{-1} DMF:DMSO = 4:1 (v/v%) solution of (FAI + PbI_2):(MABr + $PbBr_2$) = 0.87:0.13 (the amount of FAI was reduced to FAI/PbI_2 = 0.95) with CB antisolvent treatment. The details are provided in a previous report.[62,63]

https://doi.org/10.1021/jacsau.3c00519
JACS Au 2023, 3, 3194−3203

Machine Learning

Random forest (RF) modeling was performed on a notebook computer using "R studio" (free software), where a "randomForest" package and its modules (randomForest, predict, and rfcv) were used.

ASSOCIATED CONTENT

Supporting Information

The Supporting Information is available free of charge at https://pubs.acs.org/doi/10.1021/jacsau.3c00519.

Data list of automated measurements applied to device characterization (Table S1); complete list of solar cell performance (Table S2); solar cell performance with (Table S3) and without MACl additive (Table S4) at different thermal annealing temperature; solar cell performance with NH_4Cl (Table S5) or NH_4SCN (Table S6) additive; pulse shape and spectrum of white light used (Figure S1); analysis of an optical microscope image (Figure S2); picture of ∼500 samples (Figure S3); TRMC transients measured by the automated system (Figures S4−S15); photoabsorption spectra measured by the automated system (Figures S16−S27); optical microscope images measured by the automated system (Figures S28−S39); PL spectrum of a Cs−Bi−Sb−I film (Figure S40); box plots for different categories (Figure S41−S43); photoabsorption spectra and energy diagram among different Cs−Bi−Sb composition (Figure S44); XRD analyses (Figure S45); NMR analyses (Figures S46, S47); TGA results of Cs−Bi−Sb−I films (Figure S48); PY spectrum and energy diagram of the optimal film (Figure S49); cross-sectional SEM images (Figure S50); 2D-GIXRD images (Figures S51, S52); TRMC and solar cell results at different annealing temperature (Figure S53); XRD and photoabsorption spectra at different annealing temperature (Figure S54); TRMC and photoabsorption spectra of the films processed with NH_4Cl or NH_4SCN (Figure S55); *JV* curves and PCE of solar cells processed with NH_4Cl or NH_4SCN (Figure S56); XRD profiles of the films processed with NH_4Cl or NH_4SCN (Figure S57); data deviation in the automated experimental results (Figure S58); lead halide perovskite results (Figure S59); The optimal film results (Figure S60); plots of FFT-iFFT STD vs $\Delta\sigma_{max}$ plot (Figure S61); correlation among the parameters (Figure S62); RF regressions of brightness STD, $\Delta\sigma_{max}$, and E_g (Figure S63) (PDF)

Movie S1, the automated measurement system (MP4)

AUTHOR INFORMATION

Corresponding Author

Akinori Saeki − *Department of Applied Chemistry, Graduate School of Engineering, Osaka University, Suita, Osaka 565-0871, Japan; Innovative Catalysis Science Division, Institute for Open and Transdisciplinary Research Initiatives (ICS-OTRI), Osaka University, Suita, Osaka 565-0871, Japan;* orcid.org/0000-0001-7429-2200; Email: saeki@chem.eng.osaka-u.ac.jp

Authors

Chisato Nishikawa − *Department of Applied Chemistry, Graduate School of Engineering, Osaka University, Suita, Osaka 565-0871, Japan*

Ryosuke Nishikubo − *Department of Applied Chemistry, Graduate School of Engineering, Osaka University, Suita, Osaka 565-0871, Japan; Innovative Catalysis Science Division, Institute for Open and Transdisciplinary Research Initiatives (ICS-OTRI), Osaka University, Suita, Osaka 565-0871, Japan;* orcid.org/0000-0002-0533-9180

Fumitaka Ishiwari − *Department of Applied Chemistry, Graduate School of Engineering, Osaka University, Suita, Osaka 565-0871, Japan; Innovative Catalysis Science Division, Institute for Open and Transdisciplinary Research Initiatives (ICS-OTRI), Osaka University, Suita, Osaka 565-0871, Japan; PRESTO, Japan Science and Technology Agency (JST), Kawaguchi, Saitama 332-0012, Japan;* orcid.org/0000-0002-0200-4510

Complete contact information is available at: https://pubs.acs.org/10.1021/jacsau.3c00519

Author Contributions

CRediT: **Chisato Nishikawa** data curation, formal analysis, investigation, methodology, writing-original draft, writing-review & editing; **Ryosuke Nishikubo** investigation, supervision, writing-review & editing; **Fumitaka Ishiwari** validation, visualization, writing-review & editing; **Akinori Saeki** conceptualization, funding acquisition, methodology, project administration, resources, software, supervision, validation, visualization, writing-original draft, writing-review & editing.

Notes

The authors declare no competing financial interest.

ACKNOWLEDGMENTS

We acknowledge the financial support received from Core Research for Evolutional Science and Technology (CREST) (JPMJCR2107 for A.S.), MIRAI (JPMJMI22E2 for A.S.) from the Japan Science and Technology Agency (JST), the Green Innovation Project (JP21578854 for A.S.) from the New Energy and Industrial Technology Development Organization (NEDO), and KAKENHI from the Japan Society for the Promotion of Science (JSPS) (JP20H05836 and JP20H00398 for A.S. and JP22H04541, JP21H00400, and JP20H02784 for F.I.). The 2D-GIXRD experiments were conducted using proposal nos. 2022A1656 and 2022B1811. We thank Dr. Tomoyuki Koganezawa at JASRI for supporting the 2D-GIXRD experiments at SPring-8. The authors would like to thank Mr. Yohei Naito and Mr. Motohiro Kizaki of MI-6 Corp. for their technical advice and support regarding robotics.

REFERENCES

(1) Kimmig, J.; Zechel, S.; Schubert, U. S. Digital Transformation in Materials Science: A Paradigm Change in Material's Development. *Adv. Mater.* **2021**, *33*, 2004940.

(2) Wang, Z.; Sun, Z.; Yin, H.; Liu, X.; Wang, J.; Zhao, H.; Pang, C. H.; Wu, T.; Li, S.; Yin, Z.; Yu, X.-F. Data-Driven Materials Innovation and Applications. *Adv. Mater.* **2022**, *34*, 2104113.

(3) Butler, K. T.; Davies, D. W.; Cartwright, H.; Isayev, O.; Walsh, A. Machine Learning for Molecular and Materials Science. *Nature* **2018**, *559*, 547−555.

(4) Saeki, A.; Kranthiraja, K. A High Throughput Molecular Screening for Organic Electronics via Machine Learning: Present Status and Perspective. *Jpn. J. Appl. Phys.* **2020**, *59*, SD0801.

(5) Moosavi, S. M.; Jablonka, K. M.; Smit, B. The Role of Machine Learning in the Understanding and Design of Materials. *J. Am. Chem. Soc.* **2020**, *142*, 20273−20287.

(6) Häse, F.; Roch, L. M.; Friederich, P.; Aspuru-Guzik, A. Designing and Understanding Light-Harvesting Devices with Machine Learning. *Nat. Commun.* **2020**, *11*, 4587.
(7) Wang, Q.; Velasco, L.; Breitung, B.; Presser, V. High-Entropy Energy Materials in the Age of Big Data: A Critical Guide to Next-Generation Synthesis and Applications. *Adv. Energy Mater.* **2021**, *11*, 2102355.
(8) Miyake, Y.; Saeki, A. Machine Learning-Assisted Development of Organic Solar Cell Materials: Issues, Analyses, and Outlooks. *J. Phys. Chem. Lett.* **2021**, *12*, 12391−12401.
(9) Liu, Y.; Tan, X.; Liang, J.; Han, H.; Xiang, P.; Yan, W. Machine Learning for Perovskite Solar Cells and Component Materials: Key Technologies and Prospects. *Adv. Funct. Mater.* **2023**, *33*, 202214271.
(10) Xu, Y.; Liu, R.; Li, J.; Xu, Y.; Zhu, X. The Blockchain Integrated Automatic Experiment Platform (BiaeP). *J. Phys. Chem. Lett.* **2020**, *11*, 9995−10000.
(11) Dahl, C. J.; Wang, X.; Huang, X.; Chan, M. E.; Alivisatos, A. P. Elucidating the Weakly Reversible Cs-Pb-Br Perovskite Nanocrystal Reaction Network with High-Throughput Maps and Transformations. *J. Am. Chem. Soc.* **2020**, *142*, 11915−11926.
(12) Kalinin, S. V.; Ziatdinov, M.; Hinkle, J.; Jesse, S.; Ghosh, A.; Kelley, K. P.; Lupini, A. R.; Sumpter, B. G.; Vasudevan, R. K. Automated and Autonomous Experiments in Electron and Scanning Probe Microscopy. *ACS Nano* **2021**, *15*, 12604−12627.
(13) Ahmadi, M.; Ziatdinov, M.; Zhou, Y.; Lass, E. A.; Kalinin, S. V. Machine Learning for High-Throughput Experimental Exploration of Metal Halide Perovskites. *Joule* **2021**, *5*, 2797−2822.
(14) Reis, M.; Gusev, F.; Taylor, N. G.; Chung, S. H.; Verber, M. D.; Lee, Y. Z.; Isayev, O.; Leibfarth, F. A. Machine-Learning-Guided Discovery of ^{19}F MRI Agents Enabled by Automated Copolymer Synthesis. *J. Am. Chem. Soc.* **2021**, *143*, 17677−17689.
(15) Xu, S.; Liang, J.; Yu, Y.; Liu, R.; Xu, Y.; Zhu, X.; Zhao, Y. Machine Learning-Assisted Discovery of High-Voltage Organic Materials for Rechargeable Batteries. *J. Phys. Chem. C* **2021**, *125*, 21352−21358.
(16) Dave, A.; Mitchell, J.; Burke, S.; Lin, H.; Whitacre, J.; Viswanathan, V. Autonomous Optimization of Non-Aqueous Li-Ion Battery Electrolytes via Robotic Experimentation and Machine Learning Coupling. *Nat. Commun.* **2022**, *13*, 5454.
(17) Angello, N. H.; Rathore, V.; Beker, W.; Wołos, A.; Jira, E. R.; Roszak, R.; Wu, T. C.; Schroeder, C. M.; Aspuru-Guzik, A.; Grzybowski, B. A.; Burke, M. D. Closed-Loop Optimization of General Reaction Conditions for Heteroaryl Suzuki-Miyaura Coupling. *Science* **2022**, *378*, 399−405.
(18) MacLeod, B. P.; Parlane, F. G. L.; Brown, A. K.; Hein, J. E.; Berlinguette, C. P. Flexible Automation Accelerates Materials Discovery. *Nat. Mater.* **2022**, *21*, 722−726.
(19) Burger, B.; Maffettone, P. M.; Gusev, V. V.; Aitchison, C. M.; Bai, Y.; Wang, X.; Li, X.; Alston, B. M.; Li, B.; Clowes, R.; Rankin, N.; Harris, B.; Sprick, R. S.; Cooper, A. I. A Mobile Robotic Chemist. *Nature* **2020**, *583*, 237−241.
(20) MacLeod, B. P.; Parlane, F. G. L.; Morrissey, T. D.; Häse, F.; Roch, L. M.; Dettelbach, K. E.; Moreira, R.; Yunker, L. P. E.; Rooney, M. B.; Deeth, J. R.; et al. Self-Driving Laboratory for Accelerated Discovery of Thin-Film Materials. *Sci. Adv.* **2020**, *6*, No. eaaz8867.
(21) Chen, S.; Hou, Y.; Chen, H.; Tang, X.; Langner, S.; Li, N.; Stubhan, T.; Levchuk, I.; Gu, E.; Osvet, A.; Brabec, C. J. Exploring the Stability of Novel Wide Bandgap Perovskites by a Robot Based High Throughput Approach. *Adv. Energy Mater.* **2018**, *8*, 1701543.
(22) Rodríguez-Martínez, X.; Pascual-San-José, E.; Fei, Z.; Heeney, M.; Guimerà, R.; Campoy-Quiles, M. Predicting the Photocurrent-Composition Dependence in Organic Solar Cells. *Energy Environ. Sci.* **2021**, *14*, 986−994.
(23) An, N. G.; Kim, J. Y.; Vak, D. Machine Learning-Assisted Development of Organic Photovoltaics via High-Throughput in Situ Formulation. *Energy Environ. Sci.* **2021**, *14*, 3438−3446.
(24) Gómez-Bombarelli, R.; Aguilera-Iparraguirre, J.; Hirzel, T. D.; Duvenaud, D.; Maclaurin, D.; Blood-Forsythe, M. A.; Chae, H. S.; Einzinger, M.; Ha, D.-G.; Wu, T.; Markopoulos, G.; Jeon, S.; Kang, H.; Miyazaki, H.; Numata, M.; Kim, S.; Huang, W.; Hong, S. I.; Baldo, M.; Adams, R. P.; Aspuru-Guzik, A. Design of efficient molecular organic light-emitting diodes by a high-throughput virtual screening and experimental approach. *Nat. Mater.* **2016**, *15*, 1120−1127.
(25) Wu, T. C.; Aguilar-Granda, A.; Hotta, K.; Yazdani, S. A.; Pollice, R.; Vestfrid, J.; Hao, H.; Lavigne, C.; Seifrid, M.; Angello, N.; et al. A Materials Acceleration Platform for Organic Laser Discovery. *Adv. Mater.* **2023**, *34*, 2207070.
(26) Shimizu, R.; Kobayashi, S.; Watanabe, Y.; Ando, Y.; Hitosugi, T. Autonomous Materials Synthesis by Machine Learning and Robotics. *APL Mater.* **2020**, *8*, 111110.
(27) Saeki, A.; Koizumi, Y.; Aida, T.; Seki, S. Comprehensive Approach to Intrinsic Charge Carrier Mobility in Conjugated Organic Molecules, Macromolecules, and Supramolecular Architectures. *Acc. Chem. Res.* **2012**, *45*, 1193−1202.
(28) Savenije, T. J.; Ferguson, A. J.; Kopidakis, N.; Rumbles, G. Revealing the Dynamics of Charge Carriers in Polymer:Fullerene Blends Using Photoinduced Time-Resolved Microwave Conductivity. *J. Phys. Chem. C* **2013**, *117*, 24085−24103.
(29) Biondi, M. A.; Brown, S. C. Measurement of Ambipolar Diffusion in Helium. *Phys. Rev.* **1949**, *75*, 1700−1705.
(30) Warman, J. M.; Fessenden, R. W.; Bakale, G. Dissociative Attachment of Thermal Electrons to N_2O and Subsequent Electron Detachment. *J. Chem. Phys.* **1972**, *57*, 2702−2711.
(31) Grozema, F. C.; Siebbeles, L. D. A. Charge Mobilities in Conjugated Polymers Measured by Pulse Radiolysis Time-Resolved Microwave Conductivity: From Single Chains to Solids. *J. Phys. Chem. Lett.* **2011**, *2*, 2951−2958.
(32) Reid, O. G.; Moore, D. T.; Li, Z.; Zhao, D. W.; Yan, Y. F.; Zhu, K.; Rumbles, G. Quantitative Analysis of Time-Resolved Microwave Conductivity Data. *J. Phys. D* **2017**, *50*, 493002.
(33) Saeki, A. Evaluation-Oriented Exploration of Photo Energy Conversion Systems: From Fundamental Optoelectronics and Material Screening to the Combination with Data Science. *Polym. J.* **2020**, *52*, 1307−1321.
(34) Saeki, A.; Tsuji, M.; Seki, S. Direct Evaluation of Intrinsic Optoelectronic Performance of Organic Photovoltaic Cells with Minimizing Impurity and Degradation Effects. *Adv. Energy Mater.* **2011**, *1*, 661−669.
(35) Braunecker, W. A.; Oosterhout, S. D.; Owczarczyk, Z. R.; Larsen, R. E.; Larson, B. W.; Ginley, D. S.; Boltalina, O. V.; Strauss, S. H.; Kopidakis, N.; Olson, D. C. Ethynylene-Linked Donor-Acceptor Alternating Copolymers. *Macromolecules* **2013**, *46*, 3367−3375.
(36) Ponseca, C. S., Jr.; Savenije, T. J.; Abdellah, M.; Zheng, K.; Yartsev, A.; Pascher, T.; Harlang, T.; Chabera, P.; Pullerits, T.; Stepanov, A.; et al. Organometal Halide Perovskite Solar Cell Materials Rationalized: Ultrafast Charge Generation, High and Microsecond-Long Balanced Mobilities, and Slow Recombination. *J. Am. Chem. Soc.* **2014**, *136*, 5189−5192.
(37) Venkatesan, N. R.; Labram, J. G.; Chabinyc, M. L. Charge-Carrier Dynamics and Crystalline Texture of Layered Ruddlesden-Popper Hybrid Lead Iodide Perovskite Thin Films. *ACS Energy Lett.* **2018**, *3*, 380−386.
(38) Nakanishi, E.; Nishikubo, R.; Ishiwari, F.; Nakamura, T.; Wakamiya, A.; Saeki, A. Multivariate Analysis of Mixed Ternary and Quaternary A-Site Organic Cations in Tin Iodide Perovskite Solar Cells. *ACS Materials Lett.* **2022**, *4*, 1124−1131.
(39) Iyoda, F.; Nishikubo, R.; Wakamiya, A.; Saeki, A. Ag-(Bi, Sb, In, Ga)-I Solar Cells: Impacts of Elemental Composition and Additives on the Charge Carrier Dynamics and Crystal Structures. *ACS Appl. Energy Mater.* **2020**, *3*, 8224−8232.
(40) Suzuki, H.; Higashi, M.; Kunioku, H.; Abe, R.; Saeki, A. Photoconductivity-Lifetime Product Correlates Well with the Photocatalytic Activity of Oxyhalides Bi_4TaO_8Cl and $PbBiO_2Cl$: An Approach to Boost Their O_2 Evolution Rates. *ACS Energy Lett.* **2019**, *4*, 1572−1578.
(41) Kim, H.-S.; Lee, C.- R.; Im, J.- H.; Lee, K.- B.; Moehl, T.; Marchioro, A.; Moon, J. S.; Humphry-Baker, R.; Yum, J.- H.; Moser, J. E.; et al. Lead Iodide Perovskite Sensitized All-Solid-State Submicron

Thin Film Mesoscopic Solar Cell with Efficiency Exceeding 9%. *Sci. Rep.* **2012**, *2*, 591.

(42) Lee, M. M.; Teuscher, J.; Miyasaka, T.; Murakami, T. N.; Snaith, H. J. Efficient Hybrid Solar Cells Based on Meso-Superstructured Organometal Halide Perovskites. *Science* **2012**, *338*, 643−647.

(43) Yoo, J. J.; Seo, G.; Chua, M. R.; Park, T. G.; Lu, Y.; Rotermund, F.; Kim, Y.-K.; Moon, C. S.; Jeon, N. J.; Correa-Baena, J.-P.; Bulović, V.; Shin, S. S.; Bawendi, M. G.; Seo, J. Efficient Perovskite Solar Cells via Improved Carrier Management. *Nature* **2021**, *590*, 587−593.

(44) Jeong, J.; Kim, M.; Seo, J.; Lu, H.; Ahlawat, P.; Mishra, A.; Yang, Y.; Hope, M. A.; Eickemeyer, F. T.; Kim, M.; Yoon, Y. J.; Choi, I. W.; Darwich, B. P.; Choi, S. J.; Jo, Y.; Lee, J. H.; Walker, B.; Zakeeruddin, S. M.; Emsley, L.; Rothlisberger, U.; Hagfeldt, A.; Kim, D. S.; Grätzel, M.; Kim, J. Y. Pseudo-Halide Anion Engineering for α-$FAPbI_3$ Perovskite Solar Cells. *Nature* **2021**, *592*, 381−385.

(45) Kim, M.; Jeong, J.; Lu, H.; Lee, T. K.; Eickemeyer, F. T.; Liu, Y.; Choi, I. W.; Choi, S. J.; Jo, Y.; Kim, H. B.; Mo, S. I.; Kim, Y. K.; Lee, H.; An, N. G.; Cho, S.; Tress, W. R.; Zakeeruddin, S. M.; Hagfeldt, A.; Kim, J. Y.; Grätzel, M.; Kim, D. S. Conformal Quantum Dot-SnO_2 Layers as Electron Transporters for Efficient Perovskite Solar Cells. *Science* **2022**, *375*, 302−306.

(46) Park, J.; Kim, J.; Yun, H.-S.; Paik, M. J.; Noh, E.; Mun, H. J.; Kim, M. G.; Shin, T. J.; Seok, S. I. Controlled Growth of Perovskite Layers with Volatile Alkylammonium Chlorides. *Nature* **2023**, *616*, 724.

(47) Yu, B.-B.; Chen, Z.; Zhu, Y.; Wang, Y.; Han, B.; Chen, G.; Zhang, X.; Du, Z.; He, Z. Heterogeneous 2D/3D Tin-Halides Perovskite Solar Cells with Certified Conversion Efficiency Breaking 14%. *Adv. Mater.* **2021**, *33*, 2102055.

(48) Jiang, X.; Li, H.; Zhou, Q.; Wei, Q.; Wei, M.; Jiang, L.; Wang, Z.; Peng, Z.; Wang, F.; Zang, Z.; et al. One-Step Synthesis of $SnI_2\cdot(DMSO)_x$ Adducts for High-Performance Tin Perovskite Solar Cells. *J. Am. Chem. Soc.* **2021**, *143*, 10970−10976.

(49) Wang, L.; Chen, M.; Yang, S.; Uezono, N.; Miao, Q.; Kapil, G.; Baranwal, A. K.; Sanehira, Y.; Wang, D.; Liu, D.; Ma, T.; Ozawa, K.; Sakurai, T.; Zhang, Z.; Shen, Q.; Hayase, S. SnO_x as Bottom Hole Extraction Layer and Top In Situ Protection Layer Yields over 14% Efficiency in Sn-Based Perovskite Solar Cells. *ACS Energy Lett.* **2022**, *7*, 3703−3708.

(50) Ke, W.; Kanatzidis, M. G. Prospects for Low-Toxicity Lead-Free Perovskite Solar Cells. *Nat. Commun.* **2019**, *10*, 965.

(51) Attique, S.; Ali, N.; Ali, S.; Khatoon, R.; Li, N.; Khesro, A.; Rauf, S.; Yang, S.; Wu, H. A Potential Checkmate to Lead: Bismuth in Organometal Halide Perovskites, Structure, Properties, and Applications. *Adv. Sci.* **2020**, *7*, 201903143.

(52) Slavney, A. H.; Hu, T.; Lindenberg, A. M.; Karunadasa, H. I. A Bismuth-Halide Double Perovskite with Long Carrier Recombination Lifetime for Photovoltaic Applications. *J. Am. Chem. Soc.* **2016**, *138*, 2138−2141.

(53) Kim, Y.; Yang, Z.; Jain, A.; Voznyy, O.; Kim, G.-H.; Liu, M.; Quan, L. N.; García de Arquer, F. P.; Comin, F.; Fan, J. Z.; Sargent, E. H. Pure Cubic-Phase Hybrid Iodobismuthates $AgBi_2I_7$ for Thin-Film Photovoltaics. *Angew. Chem., Int. Ed.* **2016**, *55*, 9586−9590.

(54) Turkevych, I.; Kazaoui, S.; Ito, E.; Urano, T.; Yamada, K.; Tomiyasu, H.; Yamagishi, H.; Kondo, M.; Aramaki, S. Photovoltaic Rudorffites: Lead-Free Silver Bismuth Halides Alternative to Hybrid Lead Halide Perovskites. *ChemSusChem* **2017**, *10*, 3754−3759.

(55) Pantaler, M.; Cho, K. T.; Queloz, V. I. E.; Garcia Benito, I.; Fettkenhauer, C.; Anusca, I.; Nazeeruddin, M. K.; Lupascu, D. C.; Grancini, G. Hysteresis-Free Lead-Free Double-Perovskite Solar Cells by Interface Engineering. *ACS Energy Lett.* **2018**, *3*, 1781−1786.

(56) Zhu, H.; Erbing, A.; Wu, H.; Man, G. J.; Mukherjee, S.; Kamal, C.; Johansson, M. B.; Rensmo, H.; Odelius, M.; Johansson, E. M. J. Tuning the Bandgap in Silver Bismuth Iodide Materials by Partly Substituting Bismuth with Antimony for Improved Solar Cell Performance. *ACS Appl. Energy Mater.* **2020**, *3*, 7372−7382.

(57) Hu, W.; He, X.; Fang, Z.; Lian, W.; Shang, Y.; Li, X.; Zhou, W.; Zhang, M.; Chen, T.; Lu, Y.; et al. Bulk Heterojunction Gifts Bismuth-Based Lead-Free Perovskite Solar Cells with Record Efficiency. *Nano Energy* **2020**, *68*, 104362.

(58) Nishikawa, C.; Nishikubo, R.; Ishiwari, F.; Saeki, A. Combinatorial Exploration of Monovalent Metals (M, M') in Alkali, 11th-, and 13th-Group Elements toward (M/M')-(Bi/Sb)-I Solar Cells. *ACS Appl. Energy Mater.* **2022**, *5*, 6291−6301.

(59) Saeki, A.; Yoshikawa, S.; Tsuji, M.; Koizumi, Y.; Ide, M.; Vijayakumar, C.; Seki, S. A Versatile Approach to Organic Photovoltaics Evaluation Using White Light Pulse and Microwave Conductivity. *J. Am. Chem. Soc.* **2012**, *134*, 19035−19042.

(60) Nishikubo, R.; Saeki, A. Solution-Processed Bi_2S_3 Photoresistor Film To Mitigate a Trade-off between Morphology and Electronic Properties. *J. Phys. Chem. Lett.* **2018**, *9*, 5392−5399.

(61) Johansson, M. B.; Zhu, H.; Johansson, E. M. J. Extended Photo-Conversion Spectrum in Low-Toxic Bismuth Halide Perovskite Solar Cells. *J. Phys. Chem. Lett.* **2016**, *7*, 3467−3471.

(62) Jeon, N. J.; Noh, J. H.; Yang, W. S.; Kim, Y. C.; Ryu, S.; Seo, J.; Seok, S. I. Compositional Engineering of Perovskite Materials for High-Performance Solar Cells. *Nature* **2015**, *517*, 476−480.

(63) Murakami, Y.; Nishikubo, R.; Ishiwari, F.; Okamoto, K.; Kozawa, T.; Saeki, A. Exploration of Charge Transport Materials to Improve the Radiation Tolerance of Lead Halide Perovskite Solar Cells. *Mater. Adv.* **2022**, *3*, 4861−4869.

https://doi.org/10.1021/jacsau.3c00519
JACS Au 2023, 3, 3194−3203